Article

High-Temperature Corrosion Characteristics of Ni-20Cr-xSi Alloy Laser Cladding Layer in NaCl-KCl-Na$_2$SO$_4$-K$_2$SO$_4$ Mixed Salt Environment

Shanshan Chen [1,2]**, Zongde Liu** [1,]*** ID and Fulai Liu** [1]

[1] Key Laboratory of Energy Transfer and System of Power Station of Ministry of Education, North China Electric Power University, Beijing 102206, China; cjnscss@163.com (S.C.); 120222202032@ncepu.edu.cn (F.L.)

[2] Guohua Energy Investment Co., Ltd., Beijing 100007, China

* Correspondence: lzd@ncepu.edu.cn

Abstract: Ni-Cr-Si-alloy-cladding layers with Si contents of 0 wt.%, 1 wt.%, 3 wt.% and 5 wt.% were prepared via a laser-cladding technique, and the effect of Si content on the high-temperature corrosion resistance of the Ni-20Cr-Si-alloy-cladding layers in NaCl-KCl-K$_2$SO$_4$-Na$_2$SO$_4$ mixed salt was systematically investigated. The results show that at 600 °C, the four cladding layers rely mainly on the generation of dense Cr$_2$O$_3$ on the surface to hinder the continuation of corrosion. The addition of Si helps to improve the stability of Cr$_2$O$_3$ in the mixed salt, and on the other hand Si is enriched in the corrosion layer, which can effectively hinder the penetration of the corrosive medium. The addition of Si can effectively improve the high-temperature corrosion resistance of the Ni-20Cr-cladding layer, whereas the corrosion product layer is prone to spalling when the Si content is ≥3 wt.%. The best corrosion resistance was demonstrated by Ni-20Cr-1Si in NaCl-KCl-K$_2$SO$_4$-Na$_2$SO$_4$ mixed salt.

Keywords: laser cladding; Si content; Ni-Cr alloy; high-temperature corrosion

1. Introduction

The use of waste incineration for power generation not only realizes the recycling of waste-separation resources, but also achieves the purpose of environmental protection [1]. However, elements such as Cl and S contained in the waste will cause high-temperature corrosion of the boiler heating surface. The erosion of sodium, potassium, sulfate and chloride salts is an important cause of corrosion failure of heated surface materials [2,3]. High-temperature corrosion of the heating surface may eventually lead to the bursting of the tube wall, threatening the safe operation of the generating unit, which has been one of the main factors limiting the promotion and development of waste-incineration technology. Therefore, it is crucial to solve the problem of high-temperature corrosion on the heating surface of waste-incineration boilers.

Laser-cladding technology is a surface-strengthening technology in which the cladding material is placed on the substrate to be clad, and then heated using a high-energy-density laser to melt the cladding material first and then rapidly solidify it to the substrate, forming a cladding layer on the surface of the substrate material. The advantage of laser-cladding technology is that it is easy to prepare high-performance cladding layers on the surface of low-cost and low-property base materials to meet the requirements of replacing some high-performance alloys. This reduces material costs and substantially improves the performance of the base material. The corrosion-resistant cladding layer obtained on the surface of boiler tubes using laser-cladding technology can effectively prevent coating failures due to peeling. Moreover, laser-cladding technology has a lower heat input, significantly reducing the heat-affected zone of the boiler tube collective, but can also effectively prevent the dilution

rate being too high to affect the corrosion resistance of the laser-cladding layer. The laser-melting layer is metallurgically bonded to the substrate material without cracks and holes, which can significantly improve the wear and the corrosion resistance of the surface of the substrate material [4–6]. High-temperature corrosion protection using laser-melting cladding technology has received extensive attention from scholars [7–9].

In order to solve the problem of high-temperature corrosion on the heated surface of waste-incineration boilers, it is imperative to develop laser-cladding materials with better high-temperature corrosion resistance. Ni-Cr alloy can generate a Cr_2O_3 protective layer on the surface in the high-temperature corrosive environment, which makes it have better corrosion resistance and oxidation resistance [10]. However, if the Cr content is too low, a protective Cr-rich oxide layer cannot be formed on the alloy surface [11]. Increasing the Cr content will increase the brittleness of the alloy and reduce the mechanical properties of the alloy [12]. Studies have shown that the addition of appropriate amounts of Si can enhance the corrosion resistance of materials by promoting the formation of dense SiO_2 in corrosion-resistant alloys. Therefore, Si is often added to stainless steels, low-alloy steels and nickel-based alloys to improve the corrosion resistance of the alloy. Liu et al. [13] investigated the effect of Si on the corrosion resistance of weathering steels and showed that the addition of small amounts of Si contributed to the formation of network-like SiO_2, promoted the enrichment of Cr in the internal corrosion layer and improved the corrosion resistance of the alloy. Geng et al. [14] added Si to the Fe-Co-Ni alloy and showed that the addition of Si effectively reduced the oxygen partial pressure between the outer oxide layer and the substrate, promoting the selective oxidation of Cr elements and the formation of a continuous Cr_2O_3 inner oxide layer. However, no systematic study is available on the effect of Si addition on the high-temperature corrosion performance of Ni-Cr-alloy-cladding in a simulated waste-to-energy environment.

In this paper, Ni-Cr-Si-alloy-clad layers with Si content of 0 wt.%, 1 wt.%, 3 wt.% and 5 wt.% were prepared via laser-cladding technology, and the effect of Si content on the high-temperature corrosion resistance of Ni-Cr-Si-alloy-clad layers in NaCl-KCl-K2SO4-Na2SO4 mixed salt was investigated systematically and thoroughly. The role of Si in enhancing the corrosion resistance of Ni-Cr-alloy-clad layers in a simulated high-temperature corrosive environment of a waste-to-energy plant is investigated to provide a theoretical basis for solving the high-temperature corrosion problem of boiler tubes in waste-to-energy plants and the development of corrosion-resistant-clad-layer materials.

2. Materials and Methods

2.1. Laser-Cladding-Layer Preparation

Si powder was added to the Ni-20Cr-alloy powder to produce a mixture of powders with Si mass fractions of 1 wt.%, 3 wt.% and 5 wt.% in that order. It was noted that Cr powder was added accordingly to maintain the Cr content at 20 wt.%. The above three alloy powders were stirred thoroughly for 10 h to obtain a homogeneous cladding powder. Laser-cladding layers of Ni-Cr-Si alloys with different Si contents were prepared using the laser-cladding-layer technique. It has been shown that the addition of Si enhances the oxidation and corrosion resistance of the alloys even if the addition is not sufficient to form a continuous SiO_2 layer [15–17]. The Si content of most of these studies is below 5 wt.%. In addition, in the actual preparation process, it is difficult to prepare a crack-free cladding layer when the Si element addition exceeds 5 wt.%. Therefore, we chose to add Si content of not more than 5 wt.%. In order to compare the corrosion-resistance properties of cladding layers with different Si contents in more detail, we chose fused cladding layers with Si contents of 0 wt.%, 1 wt.%, 3 wt.% and 5 wt.% for comparative studies. The four cladding layers were named S0, S1, S3 and S5 according to the Si content, and the specific Ni-20Cr-xSi-alloy-powder elemental-mass fraction ratios are shown in Table 1.

Table 1. Chemical composition and nomenclature of Ni-20Cr-xSi.

Samples	Element Content (wt.%)		
	Ni	Cr	Si
S0	Bal	20	0
S1	Bal	20	1
S3	Bal	20	3
S5	Bal	20	5

The laser-cladding system mainly consists of a fiber laser, a cooling system, a synchronized-powder-feeding system and a control system. The fiber laser used in this study is a Wuhan Raycus RFL-3000 model (Wuhan Raycus Fiber Laser Technologies, Wuhan, China) with a maximum power of 3000 W and a laser spot diameter of 1.4 mm. To prevent oxidation of the alloy powder during the cladding process, argon gas (99.9%) was used to protect the powder and the molten pool, with a flow rate of 10 L/min. Nitrogen gas was used for powder feeding, with a gas flow rate of 5 L/min. The cladding powder material was uniformly dispersed around the laser beam and delivered to the molten pool in a circular powder-feeding pattern. The base material and the cladding layer were cooled by means of air cooling. To achieve smooth and continuous output of the laser, the cladding table was controlled to move and prepare multi-layer overlapped Ni-Cr-Si-alloy-cladding coatings.

To reduce the diffusion of base-metal elements into the cladding layer and minimize the dilution effect of Fe on the corrosion resistance of the cladding layer, multi-layer cladding coatings with a thickness of approximately 4–5 mm were prepared. The cladding layer was processed into a sample size of 20 mm × 10 mm × 2 mm using wire-cutting techniques (with the sample location selected in the middle-upper part of the cladding layer). The surface of the cladding-layer sample was subsequently polished using waterproof sandpaper of 400#, 600# and 800# sequentially on a metallographic polishing machine until the surface of the cladding-layer sample was smooth. The polished samples were cleaned using an ultrasonic cleaning machine in anhydrous ethanol solution for 10 min. Subsequently, the samples were subjected to ultrasonic cleaning in acetone solution for another 10 min to thoroughly remove any oil and impurities from the sample surface. After cleaning, the samples were thoroughly dried using a hot blow dryer.

2.2. High-Temperature Corrosion Test

To simulate the high-temperature corrosion environment of municipal-waste-incineration boilers, a mixture of NaCl, KCl, Na_2SO_4 and K_2SO_4 in a mass fraction ratio of 1:1:1:1 was used as the corrosive agent. High-temperature corrosion experiments were conducted within the range of 600 °C. First, the polished and cleaned cladding-layer samples were weighed and their surface areas were measured. Then, the cladding-layer samples were placed into pre-dried alumina crucibles with the mixed salt already pre-positioned. The corrosive agent was then added to cover the surface of the samples by 2–3 mm, ensuring that all surfaces of the cladding layer were covered by the mixed salt. The crucibles were placed at the central position of a tube furnace to ensure uniform heating and corrosion temperature. The duration of this corrosion experiment was 144 h.

Due to the tendency of corrosion products to easily peel off, the weight-loss method was used to measure the high-temperature corrosion resistance of the cladding layer, in order to obtain more-accurate experimental results. After corrosion, the samples were acid-washed. The acid-washing process involved removing the samples, cooling them to room temperature and cleaning off the surface corrosive agent and some corrosion products using deionized water through ultrasonic cleaning. Subsequently, 25 wt.% hydrochloric acid (concentration: 8.082 mol/L) was used for ultrasonic cleaning in a water bath at 80 °C to thoroughly remove the corrosion products from the sample surface. After the samples were thoroughly cleaned and dried, their post-corrosion masses were measured using an electronic balance (precision: ±0.01 mg) to determine the mass change after corrosion.

The corrosion weight loss per unit area of the cladding layer can be calculated using the following formula:

$$m = \frac{m_0 - m_1}{A} \tag{1}$$

where m_0 is the initial mass of the cladding-layer sample (mg), m_1 is the mass of the sample after completion of the corrosion test and removal of the surface corrosion products through acid washing (mg), and A is the original surface area of the cladding-layer sample (cm^2).

2.3. Representation

Physical analysis of the original phase composition of the cladding and corrosion products was carried out via X-ray diffraction (XRD, Raku D/Max-2400, RAMPF Tooling Solutions, Grafenberg, Germany), observation of the surface and cross-sectional morphology of the corrosion products was carried out via scanning electron microscopy (SEM, Quattro-S, FEI, Thermo Fisher Scientific, Waltham, MA, USA) and characterization of the elemental composition and distribution in typical areas was carried out via X-ray energy spectrometry (EDS, EDAX, Mahwah, NJ, USA).

3. Results

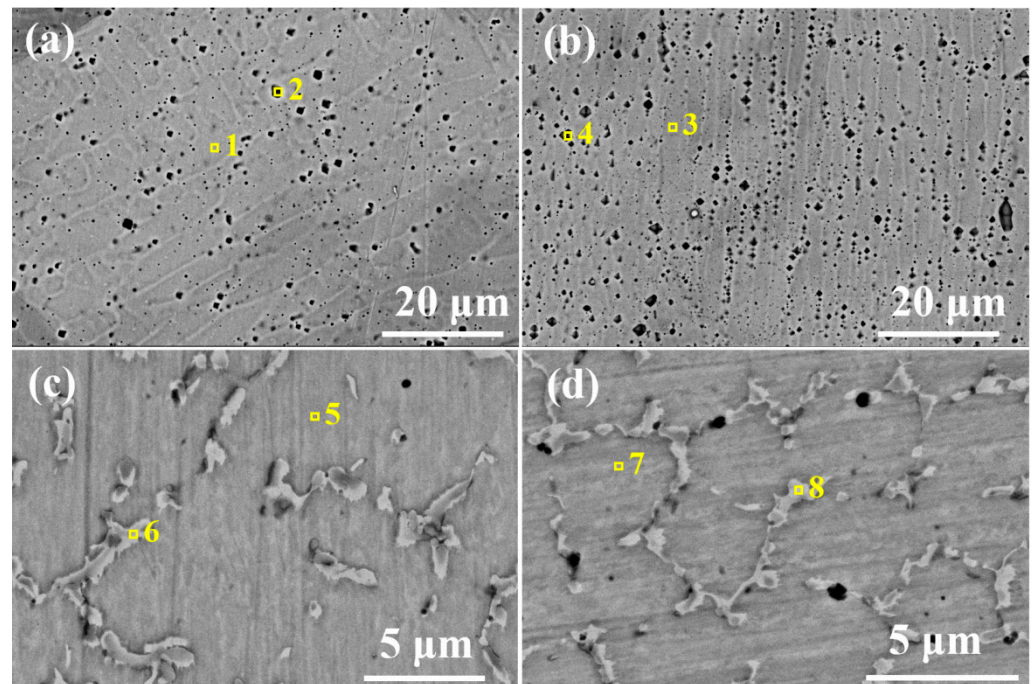### 3.1. Microstructure of Cladding Layer

Figure 1 shows the XRD diffraction patterns of Ni-Cr-Si-alloy-cladding layers of three different amounts of Si content. As shown in Figure 1, the main phase of three types of cladding layers is γ-Ni solid solution. Compared with the standard card, the diffraction peaks of three types of cladding layers all slightly shift to small angles with the increase in Si content. This is because during the laser-cladding process, the powder rapidly melts and the solidification speed of the melt pool is very fast, with most solute atoms such as Cr, Mo, Si and so on being solidly dissolved into the face-centered cubic lattice of γ-Ni. According to the Bragg equation (2dsinθ = nλ), it can be seen that due to the lattice distortion caused by the solid-solution strengthening effect, the crystal interplanar spacing of the cladding layer increases, resulting in a small angle shift of the diffraction peaks.
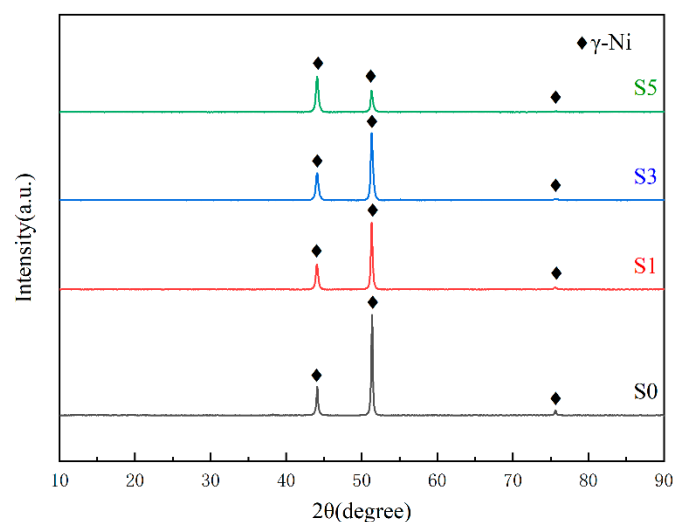
Figure 1. XRD patterns of the four cladding layers S1-S5 with different Si contents.

Figure 2 clearly shows the microstructure morphology of Ni-Cr-Si-cladding layers of four different amounts of Si content. It can be seen in the figure that the four types of cladding layers have the main characteristics of similar microstructure, mainly composed of a gray-black structure and light-white structure-like grid. At the same time, a small amount of black inclusions and pores can also be observed in the grid-like area. EDS analyses were conducted on the elemental composition of the two microstructures in the four types of cladding-layer samples, and the results show that the element content in the

two microstructures is similar (Table 2). The gray-white microstructure contains more Si, while the Ni content is relatively low. It can be inferred that the two microstructures are mainly produced by Si solidly dissolved in a γ-Ni matrix. This is because laser cladding is a rapid heating-and-cooling process with a high heat-transfer rate and solidification rate, which hinders the full diffusion of elements such as Si and so on, leading to dendritic segregation. As the Si content increases, the difference in Si content between the two microstructures becomes more significant.


Figure 2. Microstructures of cladding layers with different Si contents after etching: (**a**) S0, (**b**) S1, (**c**) S3, (**d**) S5. Marked 1–8 in the figure are the locations where EDS analysis was performed and their results are shown in Table 2.

Table 2. EDS results of typical areas in Figure 2 (in wt.%).

| wt.%	1	2	3	4	5	6	7	8
Si	-	-	0.8	3.9	7.5	7.2	7.5	11.7
Cr	22.5	24.4	23.9	22.4	20.6	29	23.5	19.9
Ni	77.5	75.6	75.4	73.7	71.9	63.8	69	68.4

3.2. Corrosion Weight Loss per Unit Area

Figure 3 reflects the weight loss of Ni-Cr-Si-alloy-cladding layers with four different Si contents after continuous corrosion at 600 °C for 144 h in a NaCl-KCl-K_2SO_4-Na_2SO_4-mixed salt. It can be known through no comparison that the corrosion resistance of the cladding layer (S1, S3, and S5) with Si addition is improved compared to the cladding layer without Si addition. When the experimental temperature is 600 °C, the order of corrosion weight loss per unit area of cladding layers with four different Si-contents from high to low is S0 > S5 > S3 > S1. The corrosion weight loss of the Ni-20Cr-alloy-cladding layer with Si addition is generally much lower than that of the cladding layer without Si addition, which indicates that Si is beneficial for improving the high-temperature corrosion resistance of the cladding layer. However, a higher Si content is not really better. The corrosion resistance of the Ni-Cr-Si-alloy-cladding layer decreases with the increase in Si content. S1 with 1 wt.% Si exhibits the best corrosion resistance.
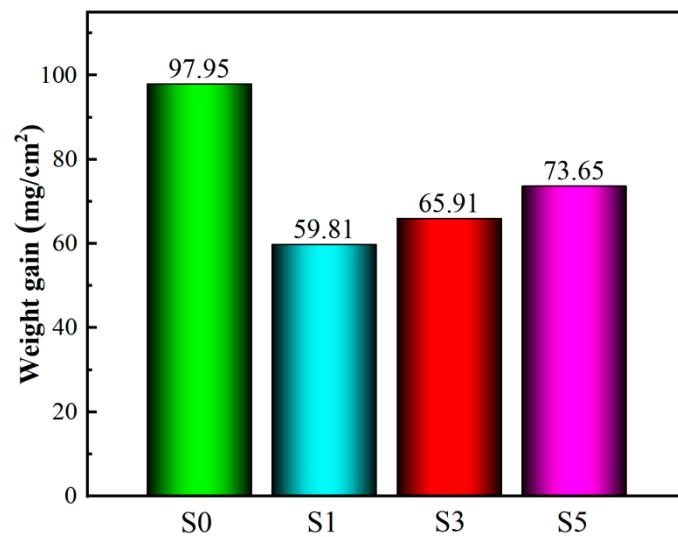
Figure 3. Weight loss of Ni-Cr-Si-alloy-cladding layers with different Si-content amounts after continuous corrosion at 600 °C in a mixed-salt solution.

3.3. Analysis about Corrosion Products

Figure 4 shows the XRD-analysis results of corrosion products of Ni-Cr-Si-alloy-cladding layers with four different Si-content amounts after corrosion for 144 h in a NaCl-KCl-K_2SO_4-Na_2SO_4 mixed salt at 600 °C. Surfaces of S0 and S1 only detected γ-Ni solid solution and Cr_2O_3 phase, while surface of S3 still detected a Ni_3S_2-corrosion product. It is worth noting that surface of S5 detected a γ-Ni-solid-solution phase, which was caused by the spalling of corrosion products, and this can be confirmed via the morphology observation of S5 corrosion products in the following passage. At the same time, SiO_2 was not detected in the corrosion products on the surface of cladding layers with Si, which indicated that during the high-temperature corrosion process, Si may accumulate in the inner corrosion layer, and the specific reasons will be discussed in detail in the analysis section on the corrosion mechanism below.
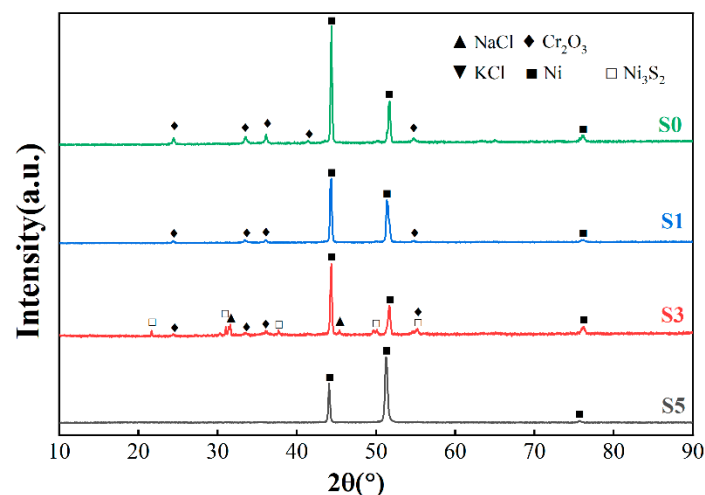

Figure 4. XRD results of corrosion products of Ni-Cr-Si-alloy-cladding layers with different Si-content amounts after continuous corrosion in mixed salt at 600 °C for 144 h.

3.4. Surface-Morphology Analysis of Corrosion Products

Figure 5 shows the surface morphologies of four different Si-content claddings after continuous corrosion for 144 h at 600 °C. As shown in Figure 5, at 600 °C, a large amount of particulate-corrosion products were formed on the surface of the S0 specimen, and

the size of the surface-particulate-corrosion products was uneven. The surface corrosion layer exhibited obvious cracking and spalling, exposing a more uniform particulate inner corrosion layer after spalling. Elemental analysis was conducted on selected regions 1 and 2 in the inner and outer corrosion layers, respectively. The results of EDS analysis (Table 3) showed that region 1 of the outer corrosion layer was mainly composed of Cr (40.4 wt.%) and O (50.7 wt.%). Combined with XRD analysis, it was determined that the outer corrosion layer was mainly composed of dense Cr_2O_3. Region 2 of the inner corrosion layer was mainly composed of Ni (72.1 wt.%) and Cr (15.4 wt.%), with elemental concentrations similar to those of the cladding matrix. Additionally, corrosive media such as O, Na and S were detected in the inner corrosion layer, indicating that once the outer oxide film was consumed, it could no longer effectively prevent the further diffusion of corrosive agents such as O, S and Cl into the cladding matrix, thereby delaying corrosion. At higher magnification, large particles were observed at the interface between the inner and outer corrosion layers. Region 3 was selected for EDS element detection, and the results showed that the elemental composition in region 3 was between regions 1 and 2, mainly consisting of Cr_2O_3 particles.
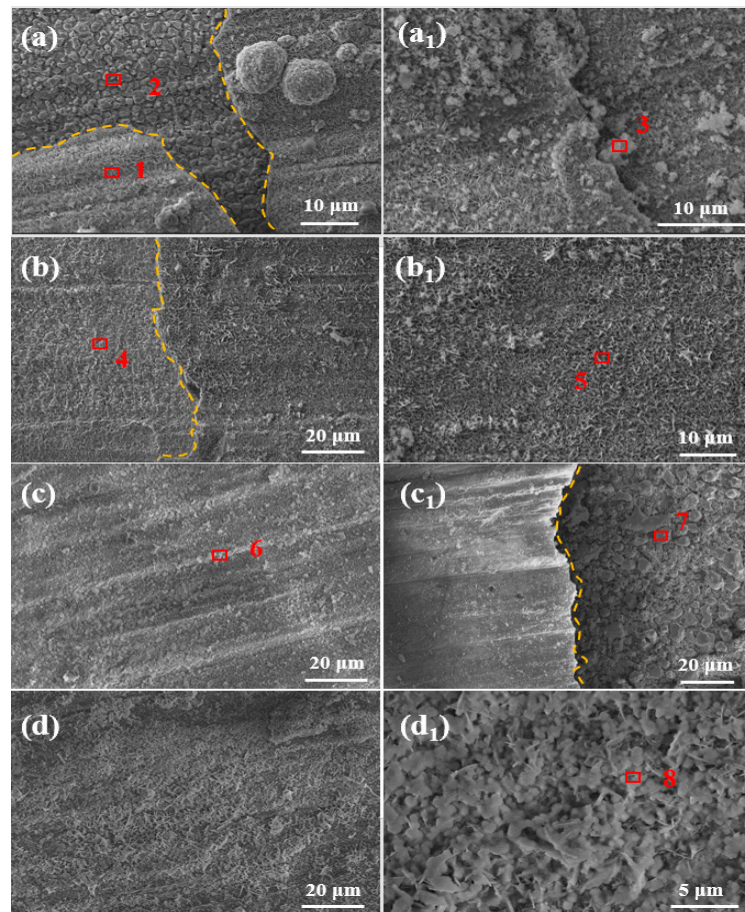
Figure 5. Surface-corrosion-product morphology of different-Si-content-cladding layers after continuous corrosion at 600 °C. (**a**) is the spalled morphology of the surface corrosion products of S0; (**a₁**) is the unspalled mor-phology of the surface corrosion products of S0; (**b**) is the spalled morphology of the surface corrosion products of S1; (**b₁**) is the unspalled morphology of the surface corrosion products of S1; (**c**) is the unspalled morphology of the surface corrosion products of S3; (**c₁**) is the spalled mor-phology of the surface corrosion products of S3; (**d**) is the morphology of the surface corrosion products of S5; (**d₁**) is the magnified morphology of the corrosion products of S5. Marked 1–8 in the figure are the locations where EDS analysis was performed and their results are shown in Table 3.

Table 3. EDS results for different regions in Figure 5 (in wt.%).

wt.%	1	2	3	4	5	6	7	8
O	50.7	8.2	34.6	0.9	40.8	26.8	1.8	32.4
Na	4.0	1.9	2.7	1.3	6.7	7.8	1.1	20.2
Si	-	-	-	2.4	0.9	3.6	0.5	2.7
S	0.7	1.2	0.8	1.1	1.9	2.7	15.9	3.9
Cl	1.2	0.6	0.8	0.4	2.3	2.4	0.4	4.1
K	1.3	0.6	1.0	0.8	1.8	3.2	0.8	6.4
Cr	40.4	15.4	52.8	10.0	39.7	41.9	2.2	24.7
Ni	1.7	72.1	7.4	83.1	6.0	11.6	77.3	5.6

3.5. Analysis of Cross-Section Morphology of Corrosion Products

The surface-corrosion morphology of S1 is shown in Figure 5. The surface appeared relatively intact and dense, with no obvious pores or cracks. Local regions exhibited protrusions. Region 4 was selected for elemental analysis, and the results showed that it was mainly composed of Ni and Cr elements, with low concentrations of other elements. This indicated that this region corresponded to the S1 substrate, demonstrating the excellent high-temperature corrosion resistance of S1. The surface corrosion layer of S1 was observed at higher magnification, revealing a dense and uniformly distributed layer with a plate-like structure. It was primarily composed of O and Cr elements, as indicated via the EDS analysis. Based on the analysis, the corrosion layer was identified as a layer of Cr_2O_3. The uniform and dense corrosion layer on the surface of S1 effectively hindered the penetration of corrosive media in the mixed salts, resulting in outstanding corrosion resistance at 600 °C.

The surface corrosion morphology of S3 is shown in Figure 5. From the figure, it can be observed that the surface of the cladding layer is denser, with no apparent pores or cracks. EDS analysis at location 6 indicated that it was mainly composed of O, Cr and Ni elements, with Si content of 3.6 wt.%. Compared to S1, the presence of corrosive elements in this area is higher, suggesting that S3 has undergone mild corrosion. Another observation revealed that the surface corrosion layer of S3 had spalled off, as shown in Figure 5c1. It is worth noting that in the exposed product layer after spalling, EDS element analysis at position 7 showed Cr content of only 2.2 wt.%, while the S content reached 15.9 wt.%. This also confirms that the corrosion resistance of S3 in the mixed salts is inferior to that of S1, as the corrosive medium S has penetrated the cladding layer matrix and reacted with it. The surface corrosion layer of S5 is shown in Figure 5d. The surface of the cladding layer appears more porous, and at higher magnifications, numerous pores can be observed in the corrosion layer, with remaining corrosion layers appearing as thin flakes. EDS results at location 8 showed that it was primarily composed of O, Cr and Na elements. During high-temperature corrosion, the surface Cr_2O_3 layer was gradually consumed, leading to the destruction of the compactness of the corrosion layer. The surface pores provided channels for the penetration of corrosive media into the interior of the cladding layer, thereby accelerating the corrosion process. The Na-element content reached 20.2 wt.%, indicating that S5 suffered severe corrosion, resulting in relatively large weight loss.

To further investigate the corrosion characteristics of Ni-20Cr-alloy claddings with different Si-content amounts in a mixed-salt environment, the cross-section morphology and elemental distribution after corrosion in $NaCl$-KCl-K_2SO_4-Na_2SO_4 mixed salt at 600 °C were observed. The EDS results for representative regions are shown in Table 4. Figures 6–9 depict the cross-sectional corrosion morphology and elemental distribution of S0, S1, S3 and S5 at 600 °C. From Figure 6, it can be seen that the surface of the S0 cladding without Si addition exhibits a porous and loose outermost layer of corrosion products, with evidence of spalling and a corrosion depth of approximately 30 μm. Three regions (1, 2 and 3) were selected for elemental analysis along the cross-section of the corrosion layer. The EDS results showed that region 1 was mainly composed of Ni (66.6 wt.%) and Cr (21.7 wt.%), indicating a low concentration of corrosive elements, suggesting that this region may correspond

to the area after the spalling of the outer corrosion layer. The dark-colored corrosion-product zone of region 2 was primarily composed of Cr and O elements, corresponding to Cr_2O_3. Region 3 exhibited elemental concentrations similar to the matrix but with a high S-element content of 11.8 wt.%, indicating severe corrosion in the S0 specimen. The elemental-distribution results revealed that the outer corrosion layer of S0 mainly consisted of Cr and O elements, with a noticeable depletion of Cr below the corrosion layer. It is worth noting that S element had penetrated into the cladding matrix, indicating severe internal corrosion. These results suggest that the cladding surface without Si addition exhibits numerous defects in the corrosion layer, which fail to effectively impede the penetration of corrosive media, resulting in severe corrosion of the cladding.

Table 4. EDS results for different regions from Figures 6–9 (in wt.%).

| wt.%	1	2	3	4	5	6	7	8	9	10	11	12	13
O	7.4	39.2	1.8	26.9	35	3.9	33.8	6.2	13.5	3.4	38.4	9.3	4.3
Na	1.7	1.7	0.5	14.8	2.6	0.9	13.3	0.8	3.4	0.3	7.5	1.7	1.0
Si	-	-	-	2.3	3.0	1.0	4.7	1.7	2.3	1.9	4.9	2.4	2.8
S	1.8	2.0	11.8	2.6	2.2	16	2.3	2.0	15.6	19.4	3.7	8.6	11.3
Cl	0.4	0.4	0.3	1.0	0.8	0.2	1.9	0.6	1.5	0.3	1.5	0.3	0.3
K	0.4	0.5	0.4	0.8	0.9	0.5	1.7	0.8	1.1	0.4	2.4	1.2	0.5
Cr	21.7	50.2	24.4	46.5	38.9	26.2	35.4	4.4	16.1	22.2	37.4	5.0	15.8
Ni	66.6	6.0	60.9	5.1	16.7	51.2	6.9	83.6	46.5	52.0	4.2	71.4	64.1
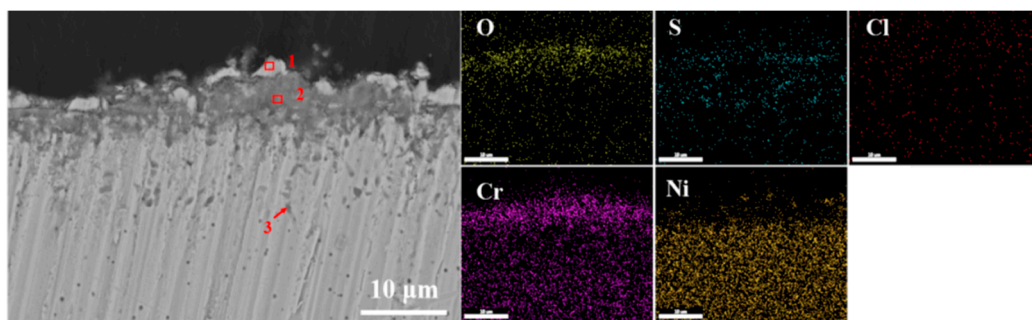
Figure 6. Cross-section morphology and elemental distribution of S0 after continuous corrosion in mixed salt at 600 °C. Marked 1–3 in the figure are the locations where EDS analysis was performed and their results are shown in Table 4.
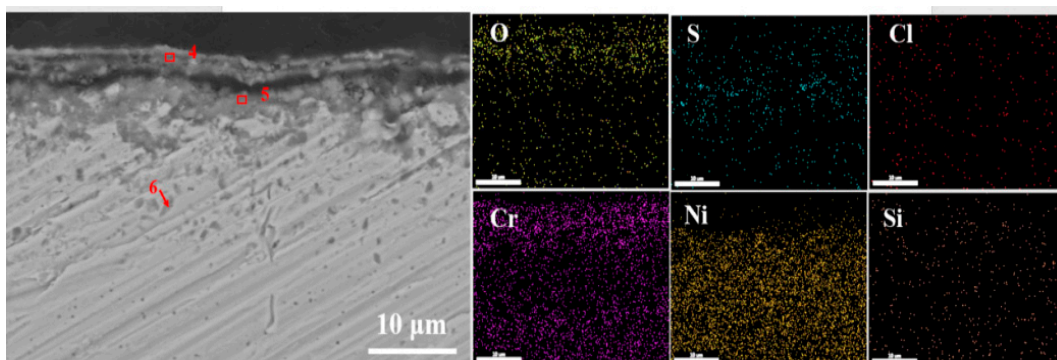
Figure 7. Cross-section morphology and elemental distribution of S1 after continuous corrosion in mixed salt at 600 °C. Marked 4–6 in the figure are the locations where EDS analysis was performed and their results are shown in Table 4.
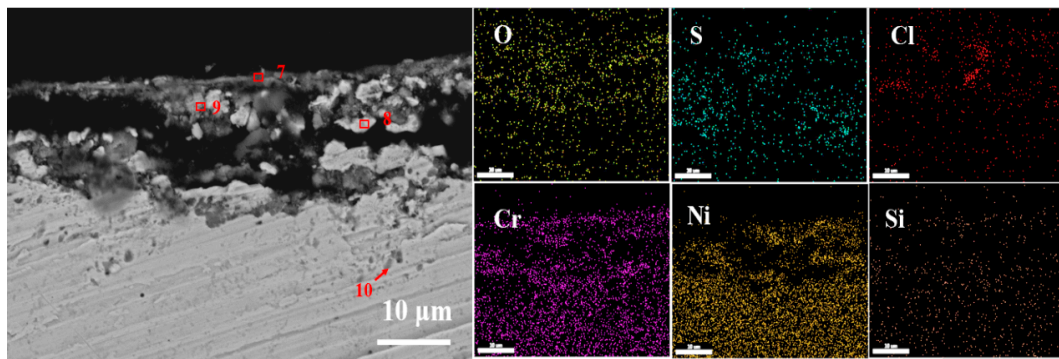
Figure 8. Cross-section morphology and elemental distribution of S3 after continuous corrosion in mixed salt at 600 °C. Marked 7–10 in the figure are the locations where EDS analysis was performed and their results are shown in Table 4.
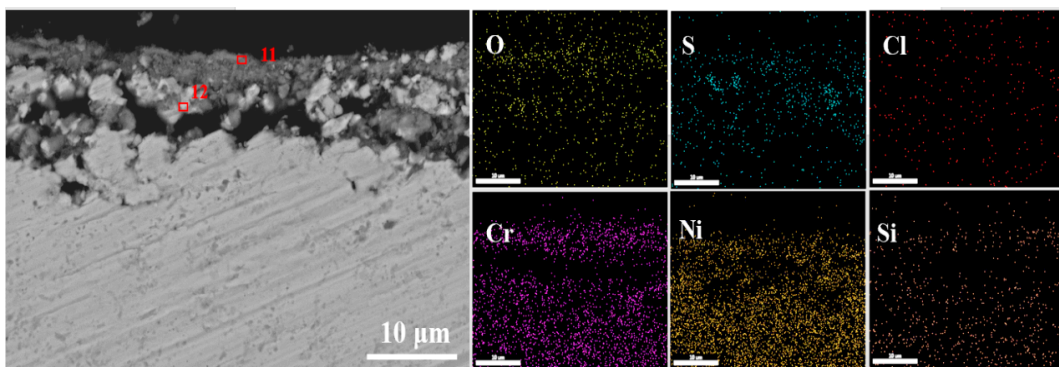
Figure 9. Cross-section morphology and elemental distribution of S5 after continuous corrosion in mixed salt at 600 °C. Marked 11–12 in the figure are the locations where EDS analysis was performed and their results are shown in Table 4.

4. Discussion

In the case of S1, a continuous corrosion layer formed on the surface, with a relatively uniform outer corrosion layer and an average thickness of approximately 5 μm. The inner corrosion layer exhibited denser corrosion products, but a clear transverse crack could be observed between the inner and outer corrosion layers, without spalling of the outer corrosion layer. Three regions (4, 5 and 6) were selected for elemental analysis along the cross-section. The EDS results showed that the outer corrosion layer was primarily composed of O (26.9 wt.%) and Cr (46.5 wt.%) elements, with a higher Na element content of 14.8 wt.%, indicating the enrichment of corrosive media in the outer corrosion layer in the mixed-salt environment. The Ni-element content increased below the crack in the inner corrosion layer, with a lower concentration of corrosive-media elements, suggesting that although there was a deep crack, the continuous outer corrosion layer effectively hindered the penetration of corrosive media. In the region near the substrate, represented by region 6, the Ni- and Cr-element contents were similar to those of the matrix, but the S element content was high at 11.8 wt.%, indicating that a small amount of S had diffused into the cladding matrix through the cracks in the surface corrosion layer, resulting in internal corrosion. The elemental-distribution results revealed that the outer corrosion layer of S1 mainly consisted of O and Cr elements, while Ni elements primarily accumulated around the inner corrosion layer.

Compared to S1, the surface morphology of the outermost corrosion-product layer changed significantly in S3 and S5, with a more porous corrosion layer, spalling of the outer corrosion layer, and the formation of numerous pores in the inner corrosion layer. The average thickness of the spalled-off region was approximately 10 μm. According to EDS element analysis, the dark-colored corrosion-product regions 7 and 11 in the outer

corrosion layer were mainly composed of O and Cr elements, confirmed via XRD analysis as predominantly Cr_2O_3. The light-colored regions 8 and 12 in the corrosion layer were primarily composed of Ni elements, with lower concentrations of O, S and Cl elements, indicating partial spalling of the outer corrosion layer and the presence of products similar to the matrix. In the molten-salt environment, the Cr_2O_3-corrosion layer formed on the surface of the cladding gradually dissolved, leading to the observation of large-scale spalling and the highest corrosion loss in S0. When SiO_2-corrosion products formed during high-temperature corrosion with the addition of Si, they partially inhibited the dissolution of the Cr_2O_3-corrosion layer, thereby impeding the penetration of corrosive media. However, when the Si content was too high, the surface corrosion layer became porous and cracked, allowing corrosive S elements to penetrate into the cladding matrix through the defects and react with the alloying elements. Region 10 in the inner corrosion layer of S3 exhibited a high S-element content of 19.4 wt.%, and XRD analysis indicated that the corrosion-product layer was mainly composed of Ni_3S_2. Furthermore, a comparison of the elemental-distribution results along the cross-section revealed that Si elements primarily accumulated in the outer corrosion layer. The addition of Si in the Ni-20Cr-alloy cladding facilitated the formation of Cr_2O_3 during high-temperature corrosion, thereby improving the corrosion resistance of the cladding layer, consistent with the observed results in this experiment.

In this experiment, O_2 can freely cross the mixed salt and react with the cladding layer, and the chemical reaction equation is as follows:
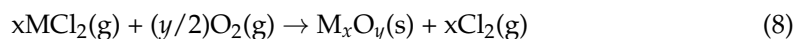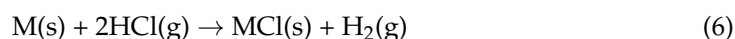
$$xM(s) + (y/2)O_2(g) \rightarrow M_xO_y(s) \tag{2}$$
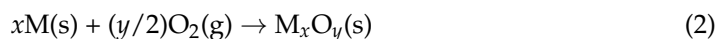
where M is Ni, Cr and other elements in the Ni-Cr-Si alloy cladding layer, the generated NiO, and Cr_2O_3 attached to the surface of the cladding layer, preventing the mixed salt and further O_2 penetration into the cladding layer, thus slowing down the process of high-temperature corrosion reaction.

In the mixed salt ($NaCl:KCl:K_2SO_4:Na_2SO_4 = 1:1:1:1$) at 600 °C, the cladding layer might undergo the following reactions during the high-temperature corrosion process:

$$RCl(s,l, g) + H_2O(g) \rightarrow ROH(s,l, g) + HCl(g) \tag{3}$$

$$4HCl(g) + O_2(g) \rightarrow 2Cl_2(g) + 2H_2O(g) \tag{4}$$
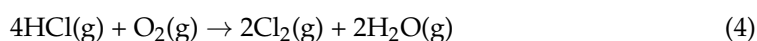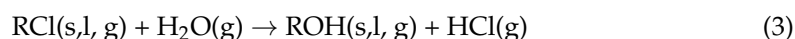
where R stands for alkali metal elements such as Na and K. The Cl_2 generated at high temperature passed through the oxide layer to the surface of the cladding layer and reacted with the metal elements to generate chlorides. This corrosion mechanism of accelerated oxidation of the alloy caused by the synergistic action of chloride and Cl_2 with O_2 is called the "active oxidation" mechanism. Therefore, the corrosion mechanism of the chloride salt in the mixed salt on the cladding layer is as follows:

$$M(s) + Cl_2(g) \rightarrow MCl_2(s) \tag{5}$$

$$M(s) + 2HCl(g) \rightarrow MCl(s) + H_2(g) \tag{6}$$

$$MCl(s) \rightarrow MCl(g) \tag{7}$$

$$xMCl_2(g) + (y/2)O_2(g) \rightarrow M_xO_y(s) + xCl_2(g) \tag{8}$$

Therefore, NiO, Cr_2O_3, etc., were detected in the S0 corrosion layer, but the product layer was loose and it was difficult to achieve the effect of hindering the corrosion medium. After adding Si to the cladding layer, SiO_2 was generated [9] (Reaction (8)) during the

high-temperature corrosion process. Although SiO_2 was not detected after corrosion, the EDS-analysis results show that SiO_2 existed in the corrosion layer, which could protect and greatly reduce the corrosion loss of the cladding layer.

$$Si + O_2 = SiO_2 \tag{9}$$

Electrochemical corrosion played a major role as the mixed salt had undergone melting [18]. A large number of studies have shown that the corrosion of the alloy will be aggravated by the addition of alkali metal chloride salts to the sulfate. This is due to the fact that NaCl and KCl can react with the Cr_2O_3 generated on the surface of the cladding layer, which reacts as follows [19]:

$$Cr_2O_3 + 4RCl + 2.5O_2(g) = 2R_2CrO_4 + 2Cl_2(g) \tag{10}$$

In addition, SO_4^- released from the sulfates (K_2SO_4 and Na_2SO_4) in the salt mixture causes the presence of O^{2-} in the molten-salt environment, with the following reaction.

$$xM(s) + ySO_4^{2-}(g, l) \rightarrow M_xO_y(s) + ySO_2 + yO^{2-} \tag{11}$$
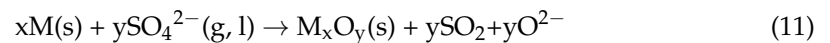
Likewise, this induces the dissolution of the Cr_2O_3 generated on the surface of the cladding layer, with the following reaction:

$$Cr_2O_3 + 2O^{2-} + 1.5O_2(g) = 2CrO_4^{2-} \tag{12}$$

The dissolved-oxide layer was loose and porous and thus not protective, resulting in a large number of cavities at the corrosion-product layer–cladding layer interface, and the corrosion layer appeared to spall off. The loose corrosion products could not block the mixed salt contact with the cladding layer, so that chloride ions could constantly consume the metal elements of the cladding layer through the above reaction. Sulfate ions could also react with the metal elements of the cladding layer to generate metal sulfides [4]. Once the corrosion layer is dissolved and does not have protective properties, Ni-sulfide particles appear between the broken oxide layer, thus causing more severe corrosion. However, the addition of a certain amount of Si to the Ni-20Cr-alloy-cladding layer significantly improves the high-temperature corrosion resistance of the cladding layer in the mixed salt. In addition, Cr_2O_3 was detected on the surface of all samples, and the cross-sectional morphology shows that a continuous Cr-rich oxide layer was attached to the surface of the cladding layer, which could provide a good protection effect. The cross-sectional morphology of the cladding layer shows that the surface of the cladding layer of the four Ni-Cr-Si alloys at all temperatures is dominated by the Cr_2O_3 layer, and the addition of Si improves the stability of Cr_2O_3 in the molten salt. Katharina et al. [20] and Wang et al. [21] pointed out that "Si can act as a nucleation site for Cr and accelerates the formation of dense Cr_2O_3 layer. Moreover, the addition of Si enhances the activity of Cr in the matrix", which is consistent with the conclusions obtained from this work. Additionally, the experimental results of Zhang et al. [22] confirmed that the presence of Si promotes the formation of a continuous dense Cr_2O_3 layer on the surface. Although a continuous SiO_2 protective layer is not generated, its presence in the corrosion layer can effectively impede the penetration of the corrosive medium, thus improving the corrosion resistance of the cladding layer in $NaCl-KCl-Na_2SO_4-K_2SO_4$ salt.

5. Conclusions

In order to further investigate the influence of Si on the high-temperature corrosion resistance of the Ni-Cr-alloy-cladding layer, Ni-20Cr-Si-alloy-cladding layers with different Si contents were prepared via laser-cladding technology. By carrying out an experiment in a mixed salt ($NaCl:KCl:K_2SO_4:Na_2SO_4 = 1:1:1:1$) at 600 °C to study the effect of Si content on the corrosion resistance of the cladding layers, the main conclusions are summarized as follows:

(1) The addition of Si can effectively improve the high-temperature corrosion resistance of the Ni-20Cr-alloy-cladding layer in a mixed salt. At 600 °C, the corrosion resistance of the four types of cladding layers is sequentially Ni-20Cr-1Si > Ni-20Cr-3Si > Ni-20Cr-5Si > Ni-20Cr-0Si.

(2) The mixed molten salt through the broken corrosion-product layer reacts with the cladding layer to accelerate corrosion, leading to an increase in corrosion weight loss of the cladding layer. The sulphate is more likely to promote the dissolution and loosening of protective metal oxides. The chloride not only damages the protective metal oxides, but also reacts to generate Cl_2, leading to an "active oxidation" mechanism.

(3) The four cladding layers mainly rely on the formation of a dense oxide layer rich in chromium (Cr_2O_3) on the surface to hinder the continuous corrosion occurring. The addition of Si is helpful to improve the stability of Cr_2O_3 in mixed salt. Moreover, Si enriched in the corrosion layer can effectively hinder the penetration of corrosion media and reduce the depth of the Cr-deficient zone. But when the Si content ≥ 3 wt.%, the corrosion product layer is prone to peeling off.

References

1. Kumar, A.; Samadder, S.R. A Review on Technological Options of Waste to Energy for Effective Management of Municipal Solid Waste. *Waste Manag.* **2017**, *69*, 407–422. [CrossRef]
2. Skrifvars, B.-J.; Backman, R.; Hupa, M.; Salmenoja, K.; Vakkilainen, E. Corrosion of Superheater Steel Materials under Alkali Salt Deposits Part 1: The Effect of Salt Deposit Composition and Temperature. *Corros. Sci.* **2008**, *50*, 1274–1282. [CrossRef]
3. Skrifvars, B.-J.; Westén-Karlsson, M.; Hupa, M.; Salmenoja, K. Corrosion of Super-Heater Steel Materials under Alkali Salt Deposits. Part 2: SEM Analyses of Different Steel Materials. *Corros. Sci.* **2010**, *52*, 1011–1019. [CrossRef]
4. Wang, X.; Liu, Z.; Cheng, K.; Kong, Y. Chlorine-Induced High-Temperature Corrosion Characteristics of Ni-Cr Alloy Cladding Layer and Ni-Cr-Mo Alloy Cladding Layer. *Corros. Sci.* **2023**, *216*, 111102. [CrossRef]
5. Zheng, C.; Liu, Z.; Liu, Q.; Li, Y.; Liu, C. Comparative Investigation on Corrosion Behavior of Laser Cladding C22 Coating, Hastelloy C22 Alloy and Ti–6Al–4V Alloy in Simulated Desulfurized Flue Gas Condensates. *J. Mater. Res. Technol.* **2022**, *18*, 2194–2207. [CrossRef]
6. Wang, X.; Liu, Z.; Cheng, K.; Shen, Y.; Li, J. Corrosion Characteristics of Inconel 625 Cladding Layer and NiCrMoAl Cladding Layer in Molten NaCl-KCl and NaCl-KCl-Na$_2$SO$_4$. *Corros. Sci.* **2023**, *221*, 111308. [CrossRef]
7. Liu, C.; Liu, Z.; Gao, Y.; Wang, X.; Zheng, C. Effect of Cr Content on Corrosion Resistance of Ni–XCr–Mo Laser-Cladding Coatings under H$_2$S-Induced High-Temperature Corrosion Atmosphere. *Materials* **2022**, *15*, 1885. [CrossRef]
8. Zheng, C.; Liu, Z.; Liu, Q.; Kong, Y.; Liu, C. Effect of Cr on Corrosion Behavior of Laser Cladding Ni-Cr-Mo Alloy Coatings in Sulfuric Acid Dew Point Corrosion Environment. *Coatings* **2022**, *12*, 421. [CrossRef]
9. Liu, S.; Liu, Z.; Wang, Y.; Tang, J. A Comparative Study on the High Temperature Corrosion of TP347H Stainless Steel, C22 Alloy and Laser-Cladding C22 Coating in Molten Chloride Salts. *Corros. Sci.* **2014**, *83*, 396–408. [CrossRef]
10. Morks, M.F.; Berndt, C.C. Corrosion and Oxidation Properties of NiCr Coatings Sprayed in Presence of Gas Shroud System. *Appl. Surf. Sci.* **2010**, *256*, 4322–4327. [CrossRef]
11. Wang, G.; Liu, H.; Chen, T.; Zhang, X.; Li, H.; Yu, Y.; Yao, H. Comparative Investigation on Thermal Corrosion of Alloy Coatings in Simulated Waste Incinerator Environment. *Corros. Sci.* **2021**, *189*, 109592. [CrossRef]
12. Hamdani, F.; Abe, H.; Ter-Ovanessian, B.; Normand, B.; Watanabe, Y. Effect of Chromium Content on the Oxidation Behavior of Ni-Cr Model Alloys in Superheated Steam. *Met. Mater. Trans. A* **2015**, *46*, 2285–2293. [CrossRef]
13. Liu, H.; Huang, F.; Yuan, W.; Hu, Q.; Liu, J.; Cheng, Y.F. Essential Role of Element Si in Corrosion Resistance of a Bridge Steel in Chloride Atmosphere. *Corros. Sci.* **2020**, *173*, 108758. [CrossRef]

14. Geng, S.; Zhu, J.; Brady, M.P.; Anderson, H.U.; Zhou, X.-D.; Yang, Z. A Low-Cr Metallic Interconnect for Intermediate-Temperature Solid Oxide Fuel Cells. *J. Power Sources* **2007**, *172*, 775–781. [CrossRef]
15. Truman, J.E.; Pirt, K.R. The Influence of the Content of Certain Incidental Elements on the Cyclic Oxidation Resistance of 12–13% Chromium Steels. *Corros. Sci.* **1976**, *16*, 103–108. [CrossRef]
16. Wang, S.; Wu, Y.; Ni, C.S.; Niu, Y. The Effect of Si Additions on the High Temperature Oxidation of a Ternary Ni–10Cr–4Al Alloy in 1 atm O_2 at 1100 °C. *Corros. Sci.* **2009**, *51*, 511–517. [CrossRef]
17. Dong, Z.; Li, M.; Behnamian, Y.; Luo, J.-L.; Chen, W.; Amirkhiz, B.S.; Liu, P.; Pang, X.; Li, J.; Zheng, W.; et al. Effects of Si, Mn on the Corrosion Behavior of Ferritic–Martensitic Steels in Supercritical Water (SCW) Environments. *Corros. Sci.* **2020**, *166*, 108432. [CrossRef]
18. Wang, J.H.; Li, D.G.; Shao, T.M. Electrochemical Study on the Hot Corrosion Behavior of $Ni_16Cr_{13}Co_4Mo$ Alloy in Molten NaCl-KCl and NaCl-KCl-Na_2SO_4. *Corros. Sci.* **2022**, *200*, 110247. [CrossRef]
19. Abu Kassim, S.; Thor, J.A.; Abu Seman, A.; Abdullah, T.K. High Temperature Corrosion of Hastelloy C22 in Molten Alkali Salts: The Effect of Pre-Oxidation Treatment. *Corros. Sci.* **2020**, *173*, 108761. [CrossRef]
20. Esleben, K.; Gorr, B.; Christ, H.-J.; Mukherji, D.; Rösler, J. The Effect of Ni and Si Additions on the Oxidation Behaviour of Co-17Re-18Cr Alloys. *Corros. Sci.* **2019**, *159*, 108135. [CrossRef]
21. Wang, Y.; Zhou, Z.; Jia, H.; Gao, R.; Ran, M.; Zheng, W.; Zhang, M.; Li, H.; Zhang, J.; Zeng, X.; et al. Understanding the Excellent Corrosion Resistance of Fe-12Cr ODS Alloys with and without Si in Supercritical CO_2 through Advanced Characterization. *Corros. Sci.* **2023**, *210*, 110827. [CrossRef]
22. Jian, Z.; Zongde, L.; Herong, M.; Yue, L.; Jiaxuan, L. Effect of Si on High Temperature Oxidation Characteristics of Laser Cladding 625 Alloy. *Rare Met. Mater. Eng.* **2022**, *51*, 3602–3610.